Supplementary Information for

Predicting Proximity-Controlled Magnetism in Two-Dimensional van der Waals Heterostructures from First Principles

Dániel Tibor Pozsár[2,*], Marcell Balázs Sípos[2], Amador García-Fuente[4,5], Péter Nemes-Incze[1], Viktor Ivády[2], Efren Navarro-Moratalla[3], Jaime Ferrer[4], László Szunyogh[6], László Oroszlány[2], and Zoltán Tajkov[1,2,*]

[1]Centre for Energy Research, Institute of Technical Physics and Materials Science, 1121 Budapest, Hungary
[2]Department of Physics of Complex Systems, ELTE Eötvös Loránd University, 1117 Budapest, Hungary
[3]Instituto de Ciencia Molecular (ICMol), Universitat de València, 46980 Spain
[4]Departamento de Física, Universidad de Oviedo, 33007 Oviedo, Spain
[5]Centro de Investigación en Nanomateriales y Nanotecnología, Universidad de Oviedo–Consejo Superior de Investigaciones Científicas, 33940 El Entrego, Spain
[6]Department of Theoretical Physics, Institute of Physics, Budapest University of Technology and Economics, Müegyetem rakpart 3., H-1111 Budapest, Hungary

[*] *Corresponding authors: daniel.pozsar@ttk.elte.hu, tajkov.zoltan@ek-cer.hu*

July 10, 2026

Contents

1 Geometry, stacking configuration, and interlayer distance

1.1 Construction and relaxation protocol

The structural model used in the main text was constructed in several steps. We first prepared separate monolayer structures for CrI_3 and hexagonal WTe_2. Both layers were initially placed in ideal high-symmetry positions in a hexagonal cell. In this starting geometry, the atomic coordinates were chosen from the ideal fractional positions of the corresponding monolayer lattices; in particular, the iodine internal coordinate of the CrI_3 ligand cage, defined below, was set to $u = 0$. The isolated CrI_3 and WTe_2 monolayers were then relaxed separately. The relaxed isolated layers were subsequently combined into a commensurate CrI_3/WTe_2 heterostructure, the relative lateral registry and interlayer distance were scanned, and the lowest-energy stacking found within this sampled structural space was selected. Finally, this selected heterostructure geometry was relaxed again using the same electronic-structure level used for the magnetic calculations, including spin–orbit coupling and the Hubbard-U correction.

The separately relaxed monolayers are nearly commensurate in the hexagonal setting used here. The relaxed primitive in-plane lattice constant of the h-WTe_2 monolayer is

$$a_{\mathrm{h-WTe_2}} = 3.570130439 \text{ Å}, \tag{1}$$

so that the doubled WTe_2 cell has

$$2a_{\mathrm{h-WTe_2}} = 7.140260878 \text{ Å}. \tag{2}$$

The relaxed in-plane lattice constant of monolayer CrI_3 is

$$a_{\mathrm{CrI_3}} = 7.130299561 \text{ Å}. \tag{3}$$

The relative lattice mismatch between the doubled h-WTe_2 cell and monolayer CrI_3 is therefore

$$\delta = \frac{2a_{\mathrm{h-WTe_2}} - a_{\mathrm{CrI_3}}}{a_{\mathrm{CrI_3}}} \times 100\% = 0.1397\%. \tag{4}$$

Thus, the two isolated monolayers can be combined in a common hexagonal simulation cell with only a very small commensuration strain. In the production heterostructure calculations we use the CrI_3 in-plane lattice constant as the common cell length, which corresponds to a compressive strain of approximately 0.14% applied to the doubled h-WTe_2 layer. This small mismatch is important for the interpretation of the magnetic anisotropy results, because it allows the WTe_2-induced spin reorientation to be discussed as a proximity effect rather than as the consequence of a large epitaxial strain.

Table 1: **Lattice matching of the separately relaxed monolayers.** The h-WTe_2 primitive cell is doubled in plane before constructing the commensurate CrI_3/WTe_2 heterostructure. The mismatch is computed as $\delta = (2a_{\mathrm{h-WTe_2}} - a_{\mathrm{CrI_3}})/a_{\mathrm{CrI_3}}$.

System	Primitive in-plane lattice constant (Å)	Matched cell length (Å)	Relative mismatch (%)
h-WTe_2	3.570130439	$2a_{\mathrm{h-WTe_2}} = 7.140260878$	+0.1397
CrI_3	7.130299561	$a_{\mathrm{CrI_3}} = 7.130299561$	reference

All energies reported for stacking comparisons were computed using the same commensurate in-plane cell and the same DFT protocol, so that the relative stacking energies are directly comparable.

1.2 Simulation cell and relaxed atomic coordinates

All calculations were performed using a hexagonal simulation cell with lattice vectors

$$\mathbf{a}_1 = (7.130299560, 0, 0)\ \text{Å}, \qquad \mathbf{a}_2 = (-3.565149780, 6.175020550, 0)\ \text{Å}, \tag{5}$$

and

$$\mathbf{a}_3 = (0, 0, 30.000000000)\ \text{Å}. \tag{6}$$

The large value of $\mathbf{a}_3$ provides the vacuum separation between periodically repeated slab images. The resulting lattice parameters are summarized in Table 2. The same in-plane cell was used for the isolated CrI_3 layer, the isolated hexagonal WTe_2 layer, and the final CrI_3/WTe_2 heterostructure. For WTe_2, we retain the doubled cell used in the heterostructure construction, since this is the actual structural model used in the calculations.

The relaxed fractional atomic coordinates of the isolated CrI_3 layer used as the structural reference are listed in Table 3. The coordinates are reported with the numerical precision used

Table 2: **Simulation-cell lattice parameters.** The same hexagonal in-plane cell was used for isolated CrI_3, isolated hexagonal WTe_2, and the CrI_3/WTe_2 heterostructure. The WTe_2 monolayer is represented in the doubled cell used in the heterostructure model.

System	N_{at}	$\lvert\mathbf{a}_1\rvert$ (Å)	$\lvert\mathbf{a}_2\rvert$ (Å)	$\lvert\mathbf{a}_3\rvert$ (Å)	γ	Cell content
CrI_3	8	7.130299560	7.130299555	30.000000000	120.000000°	2 Cr + 6 I
h-WTe_2	12	7.130299560	7.130299555	30.000000000	120.000000°	4 W + 8 Te
CrI_3/WTe_2	20	7.130299560	7.130299555	30.000000000	120.000000°	2 Cr + 6 I + 4 W + 8 Te

in the input files for reproducibility; the number of printed digits should not be interpreted as an experimentally meaningful positional accuracy at the picometre scale. The two Cr atoms lie in the central Cr plane, while the iodine atoms form the upper and lower ligand planes.

The relaxed fractional coordinates of the isolated hexagonal WTe_2 layer are given in Table 4. The WTe_2 layer is represented in the doubled cell used for the heterostructure calculations.

The final CrI_3/WTe_2 heterostructure used in the main calculations contains 20 atoms in the same simulation cell. Its relaxed fractional coordinates are listed in Table 5. In this geometry, the vertical separation between the topmost WTe_2 atom and the bottom iodine plane of CrI_3 is approximately

$$d \simeq 4.27 \text{ Å}, \tag{7}$$

when evaluated from the final relaxed coordinates. This value is consistent with the minimum of the interlayer-distance scan discussed below; small differences between the geometrical separation extracted from the relaxed coordinates and the nominal scan parameter arise from the definition of the reference atomic planes and from the final relaxation.

1.3 Internal iodine coordinate in the CrI_3 layer

The iodine positions in a CrI_3 monolayer are not completely fixed by the threefold symmetry of the Cr sublattice. In the ideal starting geometry, the iodine projections were placed at the high-symmetry fractional positions, which correspond to an internal iodine coordinate $u = 0$. During relaxation, however, the iodine cage can open or close through a symmetry-allowed internal coordinate while preserving the overall C_3-symmetric character of the CrI_3 layer.

We define the internal coordinate u from the in-plane fractional coordinates of the iodine atoms. In the present cell, the projected iodine positions can be written, up to small relaxation-induced

Table 3: **Relaxed fractional atomic coordinates of the isolated CrI_3 layer.** Coordinates are given in the simulation cell of Table 2. The atomic numbers are 24 for Cr and 53 for I.

Index	Species	Z	x	y	z
1	Cr	24	0.166660310	0.833344054	0.200625316
2	Cr	24	0.833365769	0.166641256	0.200490642
3	I	53	0.500094287	0.854655584	0.254429979
4	I	53	0.145246049	0.145371419	0.254449216
5	I	53	0.854524263	0.499816286	0.254429225
6	I	53	0.499713093	0.146012141	0.146663800
7	I	53	0.854097165	0.853750371	0.146644327
8	I	53	0.146349029	0.500382513	0.146662078

Table 4: **Relaxed fractional atomic coordinates of the isolated hexagonal WTe_2 layer.** Coordinates are given in the doubled simulation cell used for the heterostructure. The atomic numbers are 74 for W and 52 for Te.

Index	Species	Z	x	y	z
1	W	74	0.000045274	-0.000138442	-0.057129220
2	Te	52	0.166755805	0.333282338	0.004071944
3	Te	52	0.166688040	0.333241464	-0.118324251
4	W	74	0.499930884	0.000067602	-0.057129185
5	Te	52	0.666825338	0.333466379	0.004072290
6	Te	52	0.666867049	0.333440119	-0.118324202
7	W	74	0.000247634	0.500175009	-0.057129105
8	Te	52	0.166740589	0.833366786	0.004114444
9	Te	52	0.166740774	0.833366204	-0.118356291
10	W	74	0.500072249	0.500029792	-0.057141254
11	Te	52	0.666641386	0.833351634	0.004071078
12	Te	52	0.666667160	0.833419035	-0.118322965

deviations, as

$$\mathrm{I_{top}}: \quad \left(\frac{1}{2}, \frac{5}{6}+u\right), \quad \left(\frac{1}{6}-u, \frac{1}{6}-u\right), \quad \left(\frac{5}{6}+u, \frac{1}{2}\right), \tag{8}$$

$$\mathrm{I_{bottom}}: \quad \left(\frac{1}{2}, \frac{1}{6}-u\right), \quad \left(\frac{5}{6}+u, \frac{5}{6}+u\right), \quad \left(\frac{1}{6}-u, \frac{1}{2}\right). \tag{9}$$

Thus, u measures the lateral "opening" of the iodine triangles around the Cr sites in fractional coordinates. A nonzero u does not imply a loss of threefold symmetry; it simply corresponds to the symmetry-allowed relaxation of the iodine Wyckoff/internal coordinate. This is why the iodine projections need not appear as a rigid ideal sequence of perfectly 60°-separated points even when the CrI_3 layer remains effectively C_3-symmetric.

We extract u by averaging the deviations of the iodine fractional coordinates from the corresponding ideal 1/6 and 5/6 values. The resulting values are listed in Table 6. The isolated CrI_3 reference and the CrI_3 layer in the selected heterostructure have the same iodine internal coordinate within the precision of the coordinates listed above. Therefore, in the present structural model the WTe_2 substrate does not produce a sizable static distortion of the CrI_3 iodine cage. This supports the interpretation that the magnetic reorientation discussed in the main text is not driven by a large structural distortion of the CrI_3 layer, but by the electronic and relativistic proximity effect of WTe_2.

1.4 Stacking and interlayer-distance scan

After the separate relaxation of the isolated CrI_3 and WTe_2 monolayers, the two layers were combined into a CrI_3/WTe_2 heterostructure and the relative lateral registry was scanned. The lateral shift of the CrI_3 layer relative to WTe_2 was parameterized in fractional coordinates. In the older one-parameter notation used during the scan, the in-plane displacement was written as

$$\Delta \mathbf{r}_{xy} = s(\mathbf{a}_1 - \mathbf{a}_2), \tag{10}$$

which corresponds to

$$s_a = s, \qquad s_b = -s \tag{11}$$

in the two-parameter notation. The vertical separation d was defined as the distance between the topmost WTe_2 atom and the bottommost CrI_3 atom in the starting stacking models.

The final geometry used in the main text corresponds to the lowest-energy configuration found within the sampled lateral-shift and interlayer-distance scan, with

$$s_a = \frac{1}{6}, \qquad s_b = -\frac{1}{6}, \tag{12}$$

and an interlayer separation close to $d \simeq 4.4$ Å in the scan definition. This selected stacking was then used as the starting point for the final fully relativistic relaxation with the Hubbard-U correction.

Figure 1 summarizes the stacking selection. The figure shows the structural registry, the one-dimensional scan along $\Delta\mathbf{r}_{xy} = s(\mathbf{a}_1 - \mathbf{a}_2)$, the two-dimensional lateral shift scan at fixed interlayer separation, and the vertical distance scan at the selected lateral registry. The main text therefore uses a single representative heterostructure geometry, namely the lowest-energy stacking identified within this sampled structural space.

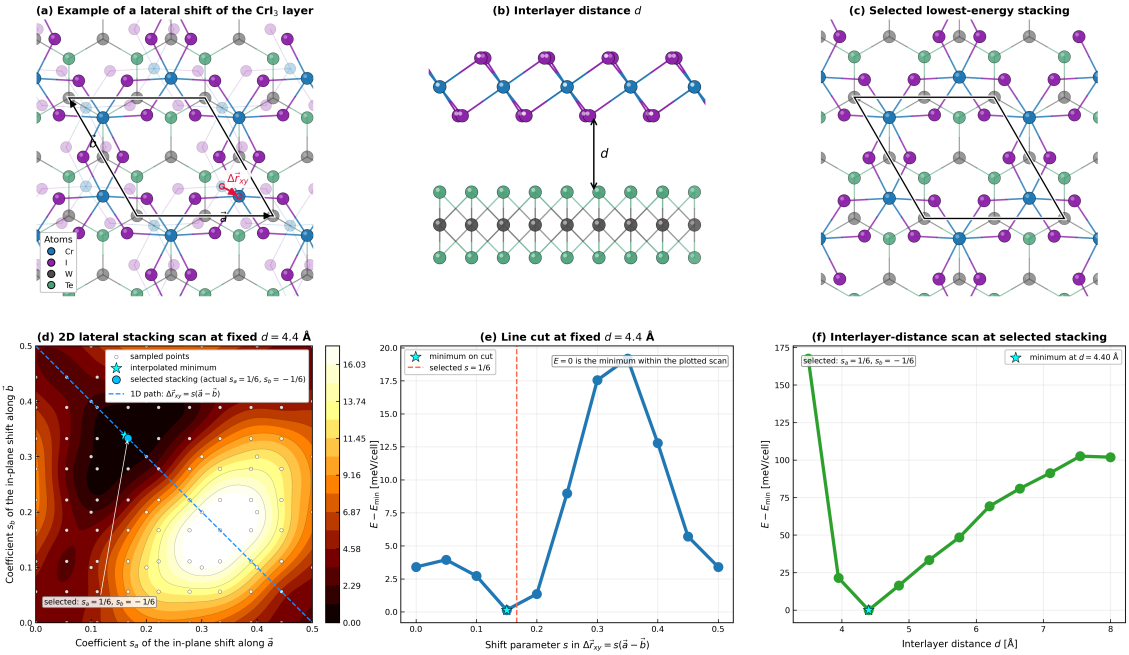

Figure 1: **Stacking geometry and relative energies of the CrI_3/WTe_2 heterostructure. a,b)** Top and side views of the selected CrI_3/WTe_2 stacking. **c)** Structural representation of the selected lowest-energy stacking within the sampled registry space. **d)** Two-dimensional lateral-shift scan along $\Delta\mathbf{r}_{xy} = s(\mathbf{a}_1 - \mathbf{a}_2)$, equivalently $s_a = s$ and $s_b = -s$, at fixed interlayer separation. **e)** One-dimensional lateral-shift scan as a function of s_a and s_b. The energy zero is set to the minimum within the sampled scan. **f)** Interlayer-distance scan at the selected lateral registry. Energies are shown as $E - E_{\min}$ in meV per simulation cell. The selected geometry corresponds to $s_a = 1/6$, $s_b = -1/6$, and an interlayer separation close to $d \simeq 4.4$ Å within the scan definition.

Table 5: **Relaxed fractional atomic coordinates of the selected CrI_3/WTe_2 heterostructure.** Coordinates are given in the common simulation cell of Table 2. Atomic numbers are 24 for Cr, 53 for I, 74 for W, and 52 for Te.

Index	Species	Z	x	y	z
1	Cr	24	0.166660310	0.833344054	0.200625316
2	Cr	24	0.833365769	0.166641256	0.200490642
3	I	53	0.500094287	0.854655584	0.254429979
4	I	53	0.145246049	0.145371419	0.254449216
5	I	53	0.854524263	0.499816286	0.254429225
6	I	53	0.499713093	0.146012141	0.146663800
7	I	53	0.854097165	0.853750371	0.146644327
8	I	53	0.146349029	0.500382513	0.146662078
9	W	74	0.000029438	-0.000204614	-0.057120430
10	Te	52	0.166782468	0.333157612	0.004088907
11	Te	52	0.166669366	0.333218802	-0.118360070
12	W	74	0.499878905	0.000077739	-0.057122629
13	Te	52	0.666950088	0.333618781	0.004089629
14	Te	52	0.666888262	0.333441607	-0.118360305
15	W	74	0.000313325	0.500228118	-0.057121177
16	Te	52	0.166738235	0.833365334	0.004219203
17	Te	52	0.166742278	0.833366666	-0.118394234
18	W	74	0.500072498	0.500033289	-0.057176197
19	Te	52	0.666490903	0.833323791	0.004088580
20	Te	52	0.666662171	0.833438887	-0.118359589

Table 6: **Internal iodine coordinate of the CrI_3 layer.** The starting high-symmetry CrI_3 geometry had $u = 0$. After relaxation, the iodine cage opens through the symmetry-allowed internal coordinate u. The last column gives $u|\mathbf{a}_1|$ as a scalar reference length for the corresponding fractional displacement.

System	Starting u	u_{top}	u_{bottom}	$\bar{u}$
CrI_3	0	0.02131	0.02054	0.02092
CrI_3/WTe_2	0	0.02131	0.02054	0.02092

Quantity	Value
Standard deviation of extracted u values	4.4×10^{-4}
$\bar{u}\|\mathbf{a}_1\|$	0.149 Å

2 Spin-orbit DFT orientation scan

To substantiate the magnetic-orientation result discussed in the main text, we performed a series of self-consistent spin–orbit-coupled DFT calculations in which the magnetic moment of the CrI_3/WTe_2 heterostructure was initialized along different in-plane azimuthal directions, as well as along the out-of-plane direction. The purpose of this scan is twofold. First, it demonstrates the robust energetic preference for an in-plane, magnetic orientation over the out-of-plane state. Second, it checks that the resulting energy landscape follows the expected rotational symmetry of the heterostructure within the practical numerical accuracy of the calculations.

For the in-plane scan we define the azimuthal angle ϕ in the plane of the CrI_3 layer. The relative energies are reported with respect to the lowest self-consistent in-plane solution,

$$\Delta E(\phi) = E(\phi) - E_{\min}, \tag{13}$$

where $E_{\min}$ is the minimum energy obtained within the scan. The out-of-plane configuration is reported on the same energy scale. Since the energy differences of interest are only a few 10^2 μeV per simulation cell, we interpret the azimuthal dependence in terms of robust energy families and the overall in-plane-versus-out-of-plane preference, rather than as a quantitatively fitted high-order anisotropy model.

Figure 2 shows the full 0°–360° azimuthal scan. The data are shown over the full angular range in order to make the approximate rotational symmetry explicit. The error bars indicate a representative numerical uncertainty of $\sigma = 80$ μeV per simulation cell, corresponding to the practical energy resolution of the self-consistent calculations. The smooth orange curve is a constrained two-harmonic fit of the form

$$E_{\mathrm{fit}}(\phi) = K_6\left[\cos(6\phi) - 1\right] + K_{12}\left[\cos(12\phi) - 1\right], \tag{14}$$

included only as a guide to the eye. It captures the qualitative periodicity of the azimuthal anisotropy, but the numerical uncertainty is too large to assign physical significance to the fitted higher-order anisotropy constants. In the main text we therefore use the DFT orientation scan only to establish the robust in-plane preference and the qualitative presence of a finite in-plane

anisotropy.

The numerical data underlying Fig. 2 are summarized in Table 7. The table also lists the final self-consistent spin direction obtained in each calculation. Most in-plane initialized calculations remain essentially in plane, with final $|S_z|$ values close to zero. The lowest-energy azimuthal family, however, develops a small out-of-plane component in some cases. This weak canting is a self-consistent SOC effect and remains small on the scale of the total Cr spin moment; it does not indicate a loss of ferromagnetic alignment of the Cr moments. The out-of-plane state remains approximately 0.35 meV per cell above the lowest in-plane solution.

The same energetic ordering is obtained from the final total energies and from the electronic free energies at the low electronic temperature used in these calculations. The differences between the two energy measures are much smaller than the orientation-energy scale relevant here, and they do not affect the conclusion that the CrI_3/WTe_2 heterostructure favors an in-plane magnetic orientation over the out-of-plane state. The small azimuthal splittings within the in-plane manifold are retained in the Supplementary Information for completeness, but they are not used in the main text to construct a quantitative in-plane anisotropy model.

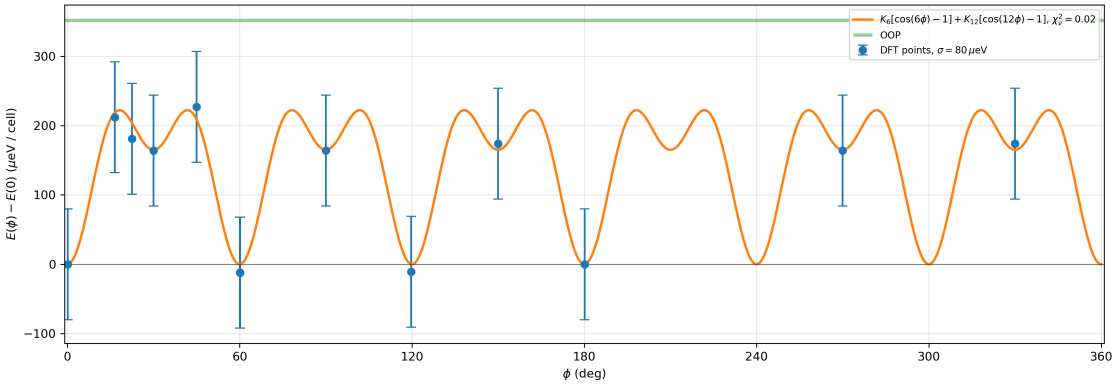

Figure 2: **Spin–orbit DFT orientation scan for the CrI_3/WTe_2 heterostructure.** Relative self-consistent SOC-DFT energies are shown as a function of the in-plane azimuthal angle ϕ, with the minimum in-plane energy set to zero. The horizontal green line marks the out-of-plane configuration. Blue points are DFT data and the error bars indicate the representative numerical uncertainty $\sigma = 80$ μeV per simulation cell. The orange line is a constrained two-harmonic guide-to-the-eye fit, $K_6[\cos(6\phi) - 1] + K_{12}[\cos(12\phi) - 1]$. The fit is not used to extract quantitative higher-order anisotropy constants. The relevant conclusion is that the out-of-plane state is higher in energy than the lowest in-plane configurations by approximately 0.35 meV per simulation cell.

Table 7: **Self-consistent SOC-DFT magnetic-orientation scan for the CrI_3/WTe_2 heterostructure.** ΔE is given relative to the minimum electronic free energy within the heterostructure orientation scan. The listed spin components are the final self-consistent total spin components reported by SIESTA. The angle ϕ_{final} is the final in-plane azimuthal direction of the spin projection, and "tilt from IP" is the absolute angular deviation from the in-plane direction. For the OOP configuration, the in-plane azimuthal angle is not physically meaningful because the in-plane spin projection is negligible.

Initial direction	ΔE (μeV/cell)	F (eV)	E_{tot} (eV)	S_x	S_y	S_z	ϕ_{final} (deg)	Tilt from IP (deg)
IP 0°	12	-6357.820075	-6357.820075	6.11474	0.01750	-0.05074	0.164	0.475
IP 15°	224	-6357.819863	-6357.819863	5.86096	1.73796	-0.09514	16.517	0.892
IP 22.5°	193	-6357.819894	-6357.819894	5.64813	2.34072	-0.00061	22.510	0.006
IP 30°	176	-6357.819911	-6357.819910	5.29484	3.05696	-0.00001	30.000	0.000
IP 45°	239	-6357.819848	-6357.819848	4.32442	4.32206	0.00100	44.984	0.009
IP 60°	0	-6357.820087	-6357.820086	3.04672	5.30173	0.05383	60.116	0.504
IP 90°	176	-6357.819911	-6357.819910	0.00004	6.11394	0.00001	90.000	0.000
IP 120°	1	-6357.820086	-6357.820086	-3.02850	5.30713	-0.23768	119.711	2.228
IP 150°	186	-6357.819901	-6357.819900	-5.29481	3.05699	-0.00002	150.000	0.000
IP 180°	12	-6357.820075	-6357.820074	-6.11483	-0.01378	0.04116	180.129	0.386
IP 270°	176	-6357.819911	-6357.819910	-0.00074	-6.11394	-0.00030	269.993	0.003
IP 330°	186	-6357.819901	-6357.819900	5.29482	-3.05695	-0.00000	330.000	0.000
OOP	352	-6357.819735	-6357.819734	0.00068	0.00117	6.11401	–	90.000

3 Projected band structures, fatbands, and PDOS

To further assess whether the proximity-induced spin reorientation is accompanied by a major reconstruction of the electronic structure, we analysed the projected band structures and projected densities of states (PDOS) of the isolated CrI_3 layer, the isolated hexagonal WTe_2 layer, and the CrI_3/WTe_2 heterostructure. The heterostructure is shown for both the representative in-plane (IP) and out-of-plane (OOP) magnetic configurations.

The band structures were calculated from the corresponding SIESTA Hamiltonians along the Γ-K-M-Γ path, using 101 points along the path. The energies are plotted relative to the Fermi energy, E_F. The PDOS was computed by Brillouin-zone averaging on a $90\times90\times1$ Monkhorst–Pack mesh using Gaussian broadening with $\sigma = 0.01$ eV.

The energy grid spans the interval $[-1, 1]$ eV around the Fermi level and contains 301 energy points, corresponding to $\Delta E = 0.0067$ eV. For the non-collinear spin–orbit calculations, the total charge component of the spin-resolved PDOS matrix was used for the orbital projections.

Figure 3 summarizes the resulting projected electronic structures. The left column shows the band structures, while the right column shows the corresponding PDOS. In the PDOS panels, the shaded backgrounds denote layer-summed contributions: CrI_3-derived states are shown in red and WTe_2-derived states in blue. The line plots show the orbital-resolved PDOS components retained above the plotting threshold. The same colour convention is used for a given orbital channel in all panels.

The isolated-layer panels provide the reference electronic structures from which the heterostructure bands can be interpreted. In isolated CrI_3, the states close to the Fermi level are dominated by Cr-d and I-p contributions. In isolated hexagonal WTe_2, the low-energy bands are primarily associated with W-d and Te-p states. In the heterostructure, these layer- and orbital-derived characters remain largely identifiable. The low-energy bands can therefore still be interpreted in terms of recognizable CrI_3- and WTe_2-derived states, rather than as a completely reconstructed electronic structure.

The finite overlap of CrI_3- and WTe_2-projected spectral weight near the Fermi level indicates weak interlayer hybridization. In particular, the heterostructure PDOS contains both Cr-d/I-p and W-d/Te-p contributions in the low-energy window. However, this mixing remains modest: the

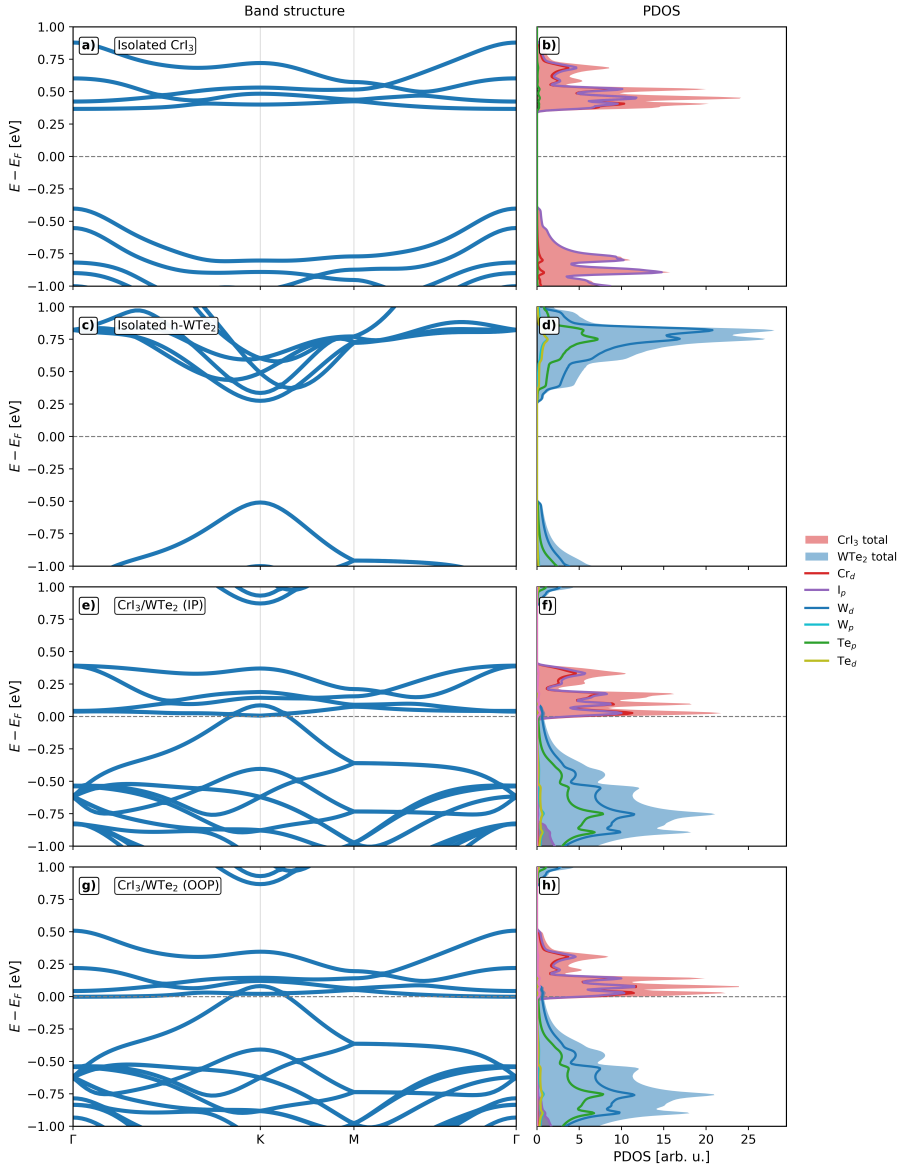

Figure 3: **Projected band structures and PDOS of isolated CrI_3, isolated h-WTe_2, and the CrI_3/WTe_2 heterostructure. a,b)** Band structure and PDOS of isolated CrI_3 in the same commensurate simulation cell used for the heterostructure construction. **c,d)** Band structure and PDOS of isolated hexagonal WTe_2 in the doubled cell used for the heterostructure. **e,f)** Band structure and PDOS of the CrI_3/WTe_2 heterostructure in the representative in-plane magnetic configuration. **g,h)** Band structure and PDOS of the CrI_3/WTe_2 heterostructure in the out-of-plane magnetic configuration. Energies are measured relative to the Fermi level. The PDOS was computed on a $90 \times 90 \times 1$ Monkhorst–Pack mesh using Gaussian broadening with $\sigma = 0.01$ eV. Shaded red and blue areas indicate the layer-summed CrI_3 and WTe_2 contributions, respectively, while solid lines show the orbital-resolved projected densities of states.

dominant layer characters remain visible, and the comparison between the IP and OOP heterostructure panels shows no large orientation-induced reconstruction of the electronic structure. This is consistent with the Mulliken population analysis in Sec. 6, which found only a small net charge transfer from WTe_2 to CrI_3 and a negligible difference between the OOP and IP layer-resolved charges.

Together, the projected band structures, PDOS, and Mulliken populations support the interpretation used in the main text: the WTe_2 substrate modifies the magnetic anisotropy of CrI_3 through a relativistic proximity effect, without strong doping of the CrI_3 layer or a major electronic reconstruction of the low-energy band structure.

4 Charge transfer and Mulliken population analysis

To assess whether the proximity-induced magnetic reorientation is accompanied by a substantial redistribution of charge, we analysed atom-projected Mulliken populations for isolated CrI_3, isolated WTe_2, and the CrI_3/WTe_2 heterostructure in both out-of-plane and in-plane magnetic configurations. The Mulliken populations were evaluated from the density and overlap matrices using the same localized-orbital basis as in the SIESTA calculations. For non-collinear spin–orbit calculations, the atom-projected Mulliken output contains the total population and the three spin components, (q, S_x, S_y, S_z), for each atom.

Mulliken populations are basis-dependent and should therefore not be interpreted as uniquely defined oxidation states. Here they are used only as an internal, consistent measure of charge redistribution within the same computational workflow. The main conclusion is that the net charge transfer between WTe_2 and CrI_3 is small, and that changing the magnetic orientation from OOP to IP produces only a very weak additional charge redistribution.

The layer-resolved Mulliken populations are summarized in Table 8. For the isolated reference systems, the CrI_3 and WTe_2 layers contain 54 and 72 Mulliken electrons, respectively, as expected from the total valence count in the simulation cell. In the heterostructure, the CrI_3 layer gains approximately $0.03e$, while the WTe_2 layer loses the same amount. The difference between the OOP and IP heterostructure calculations is only about $0.002e$ on the CrI_3 layer.

The corresponding charge transfer can be read directly from the layer-resolved populations in

Table 8: **Layer-resolved Mulliken populations and spin moments.** The first column gives the total Mulliken population on each layer. The remaining columns give the layer-summed spin components and their magnitude.

System	Layer	q	S_x	S_y	S_z	$\lvert\mathbf{S}\rvert$
isolated CrI_3	CrI_3	54.000	0.000	0.000	6.058	6.058
isolated WTe_2	WTe_2	72.000	0.000	0.000	0.000	0.000
CrI_3/WTe_2 OOP	CrI_3	54.030	0.001	0.001	6.123	6.123
CrI_3/WTe_2 OOP	WTe_2	71.970	0.000	0.000	-0.009	0.009
CrI_3/WTe_2 IP	CrI_3	54.032	5.303	3.062	0.000	6.123
CrI_3/WTe_2 IP	WTe_2	71.968	-0.008	-0.005	0.000	0.009

Table 8. Relative to the isolated layers in the same simulation cell, the CrI_3 layer gains $0.030e$ in the OOP heterostructure and $0.032e$ in the IP heterostructure, with an equal loss of Mulliken population on the WTe_2 layer. Thus,

$$\Delta q_{\mathrm{CrI_3}} \simeq +0.03e, \qquad \Delta q_{\mathrm{WTe_2}} \simeq -0.03e.$$

The difference between the OOP and IP charge transfers is only $\sim 0.002e$, far too small to indicate a substantial orientation-driven charge reconstruction. Thus the CrI_3 layer is only weakly electron-doped by the WTe_2 substrate. The small difference between the OOP and IP charge transfers, $\sim 0.002e$, is far too small to indicate a substantial orientation-driven charge reconstruction.

A species-resolved decomposition is given in Table 9. The Cr and I populations change only slightly upon forming the heterostructure. On the WTe_2 side, the Mulliken partitioning shows a redistribution between W and Te populations, but the total WTe_2 layer population changes by only $\sim 0.03e$. The induced spin polarization on WTe_2 is also very small, with a layer-summed moment of only about 0.009 in both the OOP and IP calculations. In contrast, the CrI_3 spin moment remains large and rotates consistently with the imposed magnetic orientation.

The Mulliken analysis therefore supports the interpretation used in the main text. The WTe_2 substrate induces a proximity-driven reorientation of the CrI_3 magnetization, but this reorientation is not accompanied by strong charge transfer or by a large change in the layer-resolved Mulliken populations. The charge redistribution is small on the scale of one electron per simulation cell, and the difference between OOP and IP Mulliken charges is an order of magnitude smaller still. This is consistent with a mechanism driven by relativistic proximity effects and magnetic anisotropy,

rather than by strong doping of the CrI_3 layer.

Table 9: **Species-resolved Mulliken populations.** For each species, N is the number of atoms of that species in the simulation cell, q is the species-summed Mulliken population, and q/N is the average population per atom. The spin components are summed over all atoms of the given species. Small nonzero values on W and Te represent the weak induced spin polarization of the WTe_2 layer.

System	Species	N	q	q/N	S_x	S_y	S_z	$\lvert\mathbf{S}\rvert$
isolated CrI_3	Cr	2	11.556	5.778	0.000	0.000	7.647	7.647
isolated CrI_3	I	6	42.444	7.074	0.000	0.000	-1.589	1.589
isolated WTe_2	W	4	24.245	6.061	0.000	0.000	0.000	0.000
isolated WTe_2	Te	8	47.755	5.969	0.000	0.000	0.000	0.000
CrI_3/WTe_2 OOP	Cr	2	11.570	5.785	0.001	0.002	7.713	7.713
CrI_3/WTe_2 OOP	I	6	42.460	7.077	0.000	-0.001	-1.590	1.590
CrI_3/WTe_2 OOP	W	4	24.166	6.042	0.000	0.000	-0.005	0.005
CrI_3/WTe_2 OOP	Te	8	47.803	5.975	0.000	0.000	-0.003	0.003
CrI_3/WTe_2 IP	Cr	2	11.570	5.785	6.680	3.857	0.000	7.714
CrI_3/WTe_2 IP	I	6	42.462	7.077	-1.377	-0.795	0.000	1.590
CrI_3/WTe_2 IP	W	4	24.167	6.042	-0.005	-0.003	0.000	0.006
CrI_3/WTe_2 IP	Te	8	47.801	5.975	-0.003	-0.002	0.000	0.003

5 Relativistic spin-Hamiltonian convention and tensor decomposition

The effective spin Hamiltonian extracted with GROGU is written in terms of unit vectors $\mathbf{e}_i$ along the local magnetic moments. The sign convention should be kept identical to that used in the main text and in the exported VAMPIRE files.

$$\mathcal{H} = \frac{1}{2}\sum_{ij} \mathbf{e}_i^{\mathsf{T}} \mathbf{J}_{ij} \mathbf{e}_j + \sum_i \mathbf{e}_i^{\mathsf{T}} \mathbf{K}_i \mathbf{e}_i. \tag{15}$$

The exchange tensor is decomposed into isotropic, symmetric traceless, and antisymmetric components,

$$\mathbf{J}_{ij} = J_{ij}^{\mathrm{iso}} \mathbf{I} + \mathbf{J}_{ij}^{\mathrm{S}} + \mathbf{J}_{ij}^{\mathrm{A}}. \tag{16}$$

The antisymmetric part is equivalently represented by the Dzyaloshinskii–Moriya vector $\mathbf{D}_{ij}$. For strictly collinear ferromagnetic configurations the DMI contribution vanishes because $\mathbf{e}_i \times \mathbf{e}_j = 0$.

6 VAMPIRE Monte Carlo simulation protocol and convergence

Finite-temperature magnetic ordering was studied using atomistic Monte Carlo simulations with VAMPIRE. The spin Hamiltonians were constructed from the relativistic exchange parameters obtained with the GROGU workflow and exported to VAMPIRE in tensorial form for the pair interactions. The simulations were used to determine whether the low-temperature ordered state remains out-of-plane or relaxes into an in-plane/canted-in-plane orientation, and to estimate the ordering temperature from the thermal collapse of the magnetization and the peak of the magnetic susceptibility.

The primary order parameter used in the analysis is the normalized total magnetization,

$$m(T) = \frac{|\mathbf{M}(T)|}{M_0}, \tag{17}$$

rather than a single Cartesian component. This is essential for the CrI_3/WTe_2 heterostructure, where the ordered state is in-plane or canted-in-plane. Consequently, a reduction of M_z alone is not interpreted as a loss of magnetic order. The Curie temperature was estimated from the peak position of the susceptibility $\chi_m(T)$ associated with the total magnetization, with the magnetization collapse used as a consistency check.

The standard temperature scans used

$$\Delta T = 0.5 \text{ K}, \tag{18}$$

over broad temperature intervals. Around the transition, additional fine scans were performed with

$$\Delta T = 0.25 \text{ K}. \tag{19}$$

The broad scans used 10 000 equilibration steps and 5 000 averaging steps at each temperature, while the fine scans used 20 000 equilibration steps and 20 000 averaging steps. To check numerical robustness, selected calculations were repeated for different lateral simulation sizes ($L = 30, 50, 70$ nm) and for different random seeds.

Figure 4 shows representative VAMPIRE results for isolated CrI_3 and for several CrI_3/WTe_2 Hamiltonians. Isolated CrI_3 orders out of plane and loses magnetic order around 23 K. In contrast, all representative CrI_3/WTe_2 Hamiltonians shown here remain ordered to higher temperatures and lose magnetic order in the range 33–36 K. The heterostructure simulations therefore support the DFT orientation-scan result: the WTe_2 substrate stabilizes an in-plane or canted-in-plane ordered state and increases the finite-temperature ordering scale within the same SIESTA–GROGU–VAMPIRE workflow.

The final Curie-temperature estimates extracted from the controlled VAMPIRE simulations are summarized in Table 10. The isolated CrI_3 Hamiltonian yields an out-of-plane ferromagnetic low-temperature state with $T_c \simeq 23$ K. For CrI_3/WTe_2, Hamiltonians extracted from both out-of-plane and in-plane reference calculations yield in-plane or canted-in-plane ordered states, with representative ordering temperatures in the range 33–36 K.

The stability of the extracted ordering temperatures against simulation size, random seed, and

Table 10: **Summary of VAMPIRE Curie-temperature estimates.** The reported ranges are obtained from the susceptibility peak of the total magnetization, using fine temperature scans, independent random-seed tests, and system-size checks. The low-temperature state is determined from the direction of the thermal average magnetization in the ordered phase.

System / Hamiltonian reference	Low-temperature state	T_c range (K)	Representative T_c
isolated CrI_3, OOP reference	OOP ferromagnetic	22.0–23.0	$\sim$ 23 K
CrI_3/WTe_2, OOP-reference Hamiltonian	IP/canted-IP ferromagnetic	32.5–33.75	$\sim$ 33–34 K
CrI_3/WTe_2, IP30-reference Hamiltonian	IP ferromagnetic	32.0–33.5	$\sim$ 32.5–33 K
CrI_3/WTe_2, IP45-reference Hamiltonian	IP ferromagnetic	35.0–36.0	$\sim$ 35–36 K
CrI_3/WTe_2, IP60-reference Hamiltonian	IP/canted-IP ferromagnetic	32.0–33.0	$\sim$ 32.5–33 K

temperature resolution is summarized in Table 11. The isolated CrI_3 reference remains consistently close to 23 K. The controlled heterostructure Hamiltonians remain consistently above the isolated-CrI_3 value, with IP30 and IP60 clustered near 33 K and IP45 giving a slightly higher ordering scale of about 35–36 K.

Overall, the VAMPIRE simulations provide a finite-temperature confirmation of the magnetic reorientation found at the self-consistent SOC-DFT level. Within the same spin-Hamiltonian and Monte Carlo workflow, isolated CrI_3 is an out-of-plane ferromagnet with an ordering temperature of about 23 K, whereas CrI_3/WTe_2 forms an in-plane or canted-in-plane ferromagnetic state with an ordering scale of approximately 33–36 K. The finite-temperature results therefore support the central interpretation of the main text: the WTe_2 substrate modifies the relativistic magnetic anisotropy of CrI_3 strongly enough to reorient the ordered state, while maintaining a robust ferromagnetic phase at finite temperature.

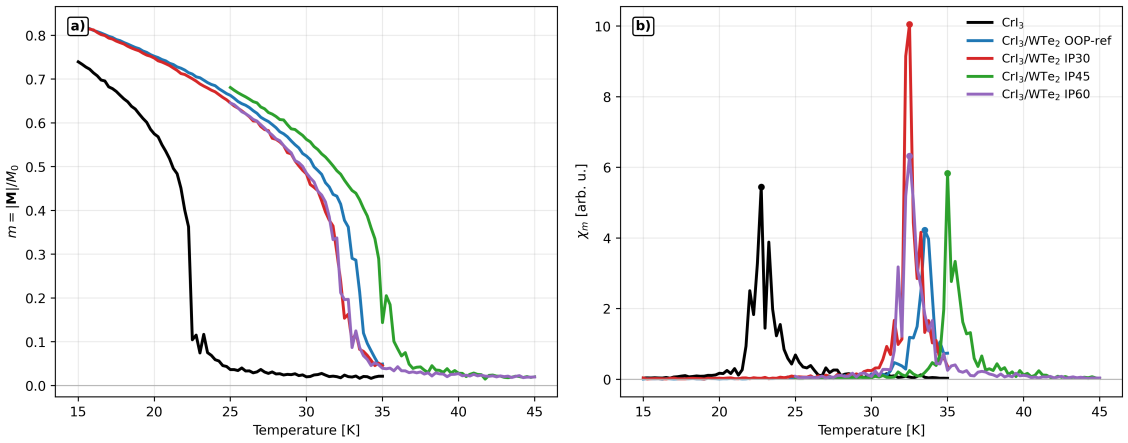

Figure 4: **Atomistic Monte Carlo simulations of isolated CrI_3 and CrI_3/WTe_2 spin Hamiltonians. a)** Normalized magnetization $m = |\mathbf{M}|/M_0$ as a function of temperature for isolated CrI_3 and for representative CrI_3/WTe_2 Hamiltonians. **b)** Corresponding susceptibility $\chi_m(T)$, used to estimate the ordering temperature. The isolated CrI_3 Hamiltonian orders at approximately 23 K, whereas the CrI_3/WTe_2 Hamiltonians show ordering temperatures in the range 33–36 K. The order parameter is the magnitude of the total magnetization, not the out-of-plane component alone.

Table 11: **Seed, size, and fine-temperature-scan controls for the VAMPIRE simulations.** For each system and control type, the table lists the range of susceptibility peak positions obtained from the corresponding controlled runs. "Seed" denotes repeated simulations with different random seeds at fixed system size, "size" denotes simulations with different lateral simulation sizes, and "fine" denotes the refined temperature scan around the transition.

System / reference	Control type	Number of runs	Parameter range	$T_c^{\chi_m}$ range (K)
isolated CrI_3 OOP	fine scan	3	$L = 50$ nm, seeds 101/202/303	22.5–23.0
isolated CrI_3 OOP	seed control	3	seeds 101/202/303	23.0–23.0
isolated CrI_3 OOP	size control	3	$L = 30/50/70$ nm	22.0–23.0
CrI_3/WTe_2 OOP-ref	fine scan	4	$L = 50$ nm, refined T grid	32.5–33.75
CrI_3/WTe_2 IP30-ref	fine scan	5	$L = 50$ nm, refined T grid	31.5–32.5
CrI_3/WTe_2 IP30-ref	seed control	3	seeds 101/202/303	32.0–33.0
CrI_3/WTe_2 IP30-ref	size control	3	$L = 30/50/70$ nm	32.0–33.5
CrI_3/WTe_2 IP45-ref	fine scan	6	$L = 50$ nm, refined T grid	34.25–35.25
CrI_3/WTe_2 IP45-ref	seed control	3	seeds 101/202/303	35.0–36.0
CrI_3/WTe_2 IP45-ref	size control	3	$L = 30/50/70$ nm	35.0–36.0
CrI_3/WTe_2 IP60-ref	fine scan	2	$L = 50$ nm, refined T grid	32.25–32.5
CrI_3/WTe_2 IP60-ref	seed control	3	seeds 101/202/303	32.5–33.0
CrI_3/WTe_2 IP60-ref	size control	3	$L = 30/50/70$ nm	32.0–33.0

7 Data availability and reproducibility

The computational data associated with this work are organized according to the three main stages of the workflow:

$$\text{SIESTA} \longrightarrow \text{GROGU} \longrightarrow \text{VAMPIRE}. \tag{20}$$

The purpose of the data package is to make the calculations reproducible while keeping the deposited dataset at a practical size. In particular, large regenerated SIESTA Hamiltonian files are not included, but the corresponding SIESTA input files, pseudopotentials, text outputs, GROGU input/output files, and VAMPIRE input/output files are provided.

The repository has the following top-level structure:

```
SIESTA/
  fdf_files/
  pseudopotentials/

GROGU/
  input_descriptions/
  pkl_outputs/

VAMPIRE/
  input_files/
  raw_outputs/
```

Each main directory contains an `index.csv` file where appropriate. These index files are intended to be the primary entry points for browsing the data. They contain repository-relative paths only, and do not contain internal server or HPC paths.

SIESTA data

The `SIESTA/fdf_files/` directory contains the SIESTA input and output files for the electronic-structure calculations used in the manuscript and in the Supplementary Information. Each selected calculation directory contains the corresponding SIESTA input file, typically `CrIWTe.fdf`, together

with the text output file named `out`. The pseudopotentials are not duplicated inside every calculation folder; instead, the pseudopotential files used throughout the study are provided once in `SIESTA/pseudopotentials/`.

The SIESTA data are grouped into subdirectories according to their role:

```
SIESTA/fdf_files/
  01_relaxations/
  02_stacking_scan/
  03_SOC_orientation_scan/
  04_isolated_CrI3_controls/
  index.csv
  missing_files_report.csv
  README.md
```

The relaxation folder contains the isolated CrI_3, isolated h-WTe_2, and selected relaxed CrI_3/WTe_2 heterostructure calculations. The stacking-scan folder contains the calculations used to identify the selected lateral registry and interlayer separation shown in Fig. 1. The spin–orbit orientation-scan folder contains the self-consistent SOC calculations used in Fig. 2 and Table 7. The isolated-CrI_3 control folder contains the corresponding magnetic-orientation calculations for CrI_3 without the WTe_2 substrate.

The `.fdf` files contain the numerical settings required to rerun the SIESTA calculations, including the basis definitions, k-point sampling, spin–orbit and non-collinear settings, Hubbard-U parameters, geometry blocks, and relaxation settings. The corresponding `.out` files provide the converged text output, including the SIESTA version information, executed calculation settings, convergence information, final energies, and reported spin and population data. Thus, the version and run-level details are preserved inside the deposited SIESTA text outputs.

The large converged SIESTA Hamiltonian files are not included in the repository because they would increase the dataset size by hundreds of gigabytes. They can, however, be regenerated from the provided `.fdf` files and pseudopotentials.

GROGU data

The `GROGU/` directory contains the spin-Hamiltonian extraction data used in the paper. GROGU takes converged SIESTA Hamiltonians as input and produces serialized output files that are subsequently used to construct the atomistic spin models. For each publication-used reference calculation, the data package includes the input script

`GROGU_input_fit.py`

and the corresponding serialized `.pkl` output file whose filename contains `fit`. Only the `generalised-fit` route used in the manuscript is included.

The included GROGU reference calculations are:

- isolated CrI_3, OOP-reference Hamiltonian,
- CrI_3/WTe_2, OOP-reference Hamiltonian,
- CrI_3/WTe_2, IP30-reference Hamiltonian,
- CrI_3/WTe_2, IP45-reference Hamiltonian,
- CrI_3/WTe_2, IP60-reference Hamiltonian.

These are the spin-Hamiltonian datasets used for the VAMPIRE calculations reported in Sec. 4. The GROGU directory contains an `index.csv` file linking each spin-Hamiltonian extraction to the corresponding SIESTA reference run identifier used in the SIESTA index.

VAMPIRE data

The `VAMPIRE/` directory contains the atomistic Monte Carlo data used to obtain the finite-temperature magnetic ordering results. The directory is split into

```
VAMPIRE/
  input_files/
  raw_outputs/
  index.csv
  missing_or_skipped_report.csv
  README.md
```

The `input_files/` directory contains a convenience copy of the VAMPIRE input and configuration files, while `raw_outputs/` contains the raw simulation outputs for the publication-used calculations. The included systems are isolated CrI_3 and the CrI_3/WTe_2 heterostructure Hamiltonians with OOP, IP30, IP45, and IP60 reference states. The VAMPIRE data include the baseline runs, fine temperature scans, random-seed controls, and size controls used to construct Table 10 and Table 11. Historical or diagnostic runs not used in the manuscript are not included.

The VAMPIRE `index.csv` file lists the system, reference state, control type, lateral simulation size, random seed, and repository-relative path to the corresponding input and output folders.

Overall, the repository is designed so that the data can be browsed from the top-level workflow directories and their `index.csv` files. To reproduce a specific result, the reader should first identify the relevant row in the corresponding index file, then use the repository-relative path to locate the calculation input or output files.